

# Wind-Ramp-Forecast Sensitivity to Closure Parameters in a Boundary-Layer Parametrization Scheme

David E. Jahn<sup>1</sup> · Eugene S. Takle<sup>2</sup> · William A. Gallus Jr.<sup>1</sup>

Received: 21 June 2016 / Accepted: 11 April 2017 / Published online: 22 April 2017  
© Springer Science+Business Media Dordrecht 2017

**Abstract** Wind ramps are relatively large changes in wind speed over a period of a few hours and present a challenge for electric utilities to balance power generation and load. Failures of boundary-layer parametrization schemes to represent physical processes limit the ability of numerical models to forecast wind ramps, especially in a stable boundary layer. Herein, the eight “closure parameters” of a widely used boundary-layer parameterization scheme are subject to sensitivity tests for a set of wind-ramp cases. A marked sensitivity of forecast wind speed to closure-parameter values is observed primarily for three parameters that influence in the closure equations the depth of turbulent mixing, dissipation, and the transfer of kinetic energy from the mean to the turbulent flow. Reducing the value of these parameters independently by 25% or by 50% reduces the overall average in forecast wind-speed errors by at least 24% for the first two parameters and increases average forecast error by at least 63% for the third parameter. Doubling any of these three parameters increases average forecast error by at least 67%. Such forecast sensitivity to closure parameter values provides motivation to explore alternative values in the context of a stable boundary layer.

**Keywords** Boundary-layer parametrization · Wind-speed forecasts · Wind ramps

## 1 Introduction

Accurate forecasts of wind speed at turbine-hub height are crucial if wind power is to be a viable and dependable source of electric power. Wind speed, however, is highly variable, and large fluctuations over a relatively short period of time (wind ramps) can have a significant

---

✉ David E. Jahn  
djahn@iastate.edu

<sup>1</sup> Department of Geological and Atmospheric Sciences, Iowa State University, 253 Science, Ames, IA 50011, USA

<sup>2</sup> Department of Agronomy, 2104 Agronomy Hall, Iowa State University, 253 Science, Ames, IA 50011, USA

impact on utility operations, for which power generation and load must remain in balance. Failures of planetary boundary-layer (PBL) parametrization schemes to represent physical processes, such as the evolution of turbulent variances, limit the ability of numerical weather prediction models to forecast wind ramps, especially in a stable boundary layer (SBL). In the Mellor–Yamada–Nakanishi–Niino (MYNN) 1.5-order closure scheme (Mellor 1973; Mellor and Yamada 1974, 1982; Nakanishi 2001; Nakanishi and Niino 2004 hereafter referred to as M73, MY74, MY82, N01, and NN04 respectively), the relative influence of each energy term in the equations that solve for turbulent fluxes is dictated by arbitrary and pre-defined weighting constants, or “closure parameters”. The focus here is on the sensitivity of mesoscale-model wind-ramp forecasts to systematic variations of the MYNN-scheme closure parameters, specifically for wind-ramp events in a SBL. We consider the MYNN level-3.0 scheme in the Weather Research Forecast (WRF) model (Skamarock et al. 2008).

Wind ramps are generally defined as a 50% change in wind generation as compared to total-power capacity within a period of 4 h or less. Although a relatively strong change in wind speed can be caused by a frontal passage or by the gust front of a nearby storm, wind ramps are also associated with the onset of a nocturnal low-level jet (LLJ; Greaves et al. 2009; Deppe et al. 2013).

In reference to wind-ramp forecasts, a Mid-continent Independent System Operator (MISO) report (Navid et al. 2011) indicated a wind-generation day-ahead forecast error in the MISO region of 8–10% of wind-generation capacity, which represents up to 30% of actual wind generation. Another study, based on 15 months of commercially-available day-ahead forecasts for a set of sites in the USA and the UK, reported an accuracy of 30–35% in predicting wind-ramp events (Greaves et al. 2009). For a wind-farm site in Iowa, Deppe et al. (2013) found that mesoscale-model simulations with a 30-h forecast horizon correctly predicted approximately only 50% of wind ramps within a margin of 6 h of actual occurrence.

In addressing forecast-model inaccuracies of wind ramps and wind speed, several studies agree that a focus on PBL parametrization schemes is necessary (Schreck et al. 2008; Storm and Basu 2010; Grisogono 2010; Fernando and Weil 2010; Hu et al. 2013; Deppe et al. 2013). These studies found that commonly-used PBL schemes do not represent well specific dynamics associated with wind ramps, including the strength of the LLJ or the nocturnal cooling of the lower atmosphere.

The closure parameters in the current MYNN scheme do not change regardless of environmental conditions. The purpose here is to investigate the viability of improving WRF-model wind-ramp forecasts by documenting forecast sensitivity to systematic changes in the closure parameters. The MYNN scheme has been chosen because it is a widely used option in the WRF model for both operational runs by the US National Weather Service (Benjamin et al. 2013) and within the research community.

The fundamental basis of the MYNN scheme is summarized in Sect. 2. Section 3 describes the methodology for setting up a series of sensitivity experiments using the WRF model by systematically varying closure-parameter values among a suite of select wind-ramp cases. Section 4 presents the results of these sensitivity experiments, with more in-depth analyses of specific cases given in Sect. 5. Section 6 provides a summary of results and implications for future work.

## 2 Basic Theory of the MYNN Scheme

The MYNN PBL parametrization scheme is based on the following conservation equations that are similar to those given in M73, MY74, and MY82,

$$\frac{\partial U_k}{\partial x_k} = 0, \tag{1}$$

$$\frac{\partial U_j}{\partial t} + \frac{\partial}{\partial x_k} (U_k U_j + \overline{u_k u_j}) + \epsilon_{jkl} f_k U_l = -\frac{1}{\rho} \frac{\partial P}{\partial x_j} - g \delta_{j3} \beta \Theta + \nu \nabla^2 U_j, \tag{2}$$

and

$$\frac{\partial \Theta}{\partial t} + \frac{\partial}{\partial x_k} (U_k \Theta + \overline{u_k \theta}) = \alpha \nabla^2 \Theta, \tag{3}$$

for which Einstein summation notation has been adopted. Here  $U_j$ ,  $\Theta$ , and  $P$  are the mean values of wind speed, potential temperature, and pressure respectively, while  $u_j$ ,  $\theta$ , and  $p$  are respective fluctuations about the mean. Expressions with an overbar represent Reynolds averaged values. Also,  $g$  represents the (vertical) gravity vector,  $f$  is the Coriolis parameter, and  $\beta$  the coefficient of thermal expansion ( $\beta = -(\partial\rho/\partial T)/\rho$ ) while  $\nu$  represents kinematic viscosity and  $\alpha$  is the kinematic heat conductivity.

The turbulent momentum and heat fluxes,  $\overline{u_i u_j}$ ,  $\overline{u_i \theta}$ , and  $\overline{\theta^2}$ , represent 10 combinations of variables, which are determined by a system of equations, given here in loose form,

$$\frac{\partial \overline{u_i u_j}}{\partial t} + \frac{\partial (U_k \overline{u_i u_j})}{\partial x_k} + \overline{u_k u_i} \frac{\partial U_j}{\partial x_k} + \overline{u_k u_j} \frac{\partial U_i}{\partial x_k} = E_{distr} + E_{diff} + E_{disp} + E_{buoy} + F, \tag{4}$$

where  $E_{distr}$ ,  $E_{diff}$ , and  $E_{disp}$  are energy distribution, diffusion, and dispersion terms while  $E_{buoy}$  and  $F$  are the buoyancy and Coriolis terms; and,

$$\frac{\partial \overline{u_j \theta}}{\partial t} + \frac{\partial (U_k \overline{u_j \theta})}{\partial x_k} + \overline{u_j u_k} \frac{\partial \Theta}{\partial x_k} + \overline{\theta u_k} \frac{\partial U_j}{\partial x_k} = H_{distr} + H_{disp} + H_{diff} + H_{buoy}. \tag{5}$$

Here  $H_{distr}$ ,  $H_{disp}$ , and  $H_{diff}$  denote energy distribution, dissipation, and diffusion terms associated with the heat flux, and  $H_{buoy}$  represents buoyancy effects. Also

$$\frac{\partial \overline{\theta^2}}{\partial t} + \frac{\partial (U_k \overline{\theta^2})}{\partial x_k} + 2\overline{u_k \theta} \frac{\partial \Theta}{\partial x_k} = T_{disp} + T_{diff}, \tag{6}$$

such that terms on the right-hand side (r.h.s.) represent energy dissipation and diffusion respectively.

This system requires solving ten differential equations that determine the evolution of the suite of turbulent momentum and heat fluxes including  $\overline{u\overline{w}}$ ,  $\overline{v\overline{w}}$ ,  $\overline{u\overline{v}}$ ,  $\overline{u\overline{\theta}}$ ,  $\overline{v\overline{\theta}}$ ,  $\overline{w\overline{\theta}}$ , the divergence of which influences the forecast of the mean flow per the third term on the left-hand side (l.h.s.) of Eq. 2.

By invoking the boundary-layer approximation and neglecting time-tendency, diffusion, and Coriolis terms (consistent with the approach in M73, MY74, and MY82), this system of prognostic equations (Eqs. 4, 5), is transformed into a list of diagnostic equations,

$$\overline{u^2} = \frac{q^2}{3} + \frac{A_1 L}{q} \left\{ -4\overline{uw} \frac{\partial U}{\partial z} + 2\overline{vw} \frac{\partial V}{\partial z} - 2\beta g \overline{w\theta} + 2C_2 \beta g \overline{w\theta} \right\}, \tag{7}$$

$$\overline{v^2} = \frac{q^2}{3} + \frac{A_1 L}{q} \left\{ 2\overline{uw} \frac{\partial U}{\partial z} - 4\overline{vw} \frac{\partial V}{\partial z} - 2\beta g \overline{w\theta} + 2C_2 \beta g \overline{w\theta} \right\}, \tag{8}$$

$$\overline{w^2} = \frac{q^2}{3} + \frac{A_1 L}{q} \left\{ 2\overline{uw} \frac{\partial U}{\partial z} + 2\overline{vw} \frac{\partial V}{\partial z} + 4\beta g \overline{w\theta} - 4C_2 \beta g \overline{w\theta} \right\}, \tag{9}$$

$$\overline{uv} = \frac{3A_1 L}{q} \left\{ -\overline{uw} \frac{\partial V}{\partial z} - \overline{vw} \frac{\partial U}{\partial z} \right\}, \tag{10}$$

$$\overline{uw} = \frac{3A_1 L}{q} \left\{ -\overline{w^2} \frac{\partial U}{\partial z} + \beta g \overline{u\theta} + C_1 q^2 \frac{\partial U}{\partial z} - C_2 \beta g \overline{u\theta} \right\}, \tag{11}$$

$$\overline{vw} = \frac{3A_1 L}{q} \left\{ -\overline{w^2} \frac{\partial V}{\partial z} + \beta g \overline{v\theta} + C_1 q^2 \frac{\partial V}{\partial z} - C_2 \beta g \overline{v\theta} \right\}, \tag{12}$$

$$\overline{u\theta} = -\frac{3LA_2}{q} \left[ \overline{uw} \frac{\partial \Theta}{\partial z} + \overline{w\theta} \frac{\partial U}{\partial z} (1 - C_5) \right], \tag{13}$$

$$\overline{v\theta} = -\frac{3LA_2}{q} \left[ \overline{vw} \frac{\partial \Theta}{\partial z} + \overline{w\theta} \frac{\partial V}{\partial z} (1 - C_5) \right], \tag{14}$$

and

$$\overline{w\theta} = -\frac{3LA_2}{q} \left[ \overline{w^2} \frac{\partial \Theta}{\partial z} + \overline{w\theta} \frac{\partial w}{\partial z} + g\beta \overline{\theta^2} \right] - C_3 g \beta \overline{\theta^2} - C_5 \overline{w\theta} \frac{\partial w}{\partial z}. \tag{15}$$

The full system of equations for the MYNN scheme consists also of two prognostic equations, the first being

$$\frac{Dq^2/2}{Dt} - \frac{\partial}{\partial z} \left[ LqS_q \frac{\partial q^2/2}{\partial z} \right] = -\overline{uw} \frac{\partial U}{\partial z} - \overline{vw} \frac{\partial V}{\partial z} + \beta g \overline{w\theta} - \frac{q^3}{B_1 L}, \tag{16}$$

where  $q^2 = \overline{u^2}$  such that turbulent kinetic energy (TKE) is  $q^2/2$ , and the second is

$$\frac{D\overline{\theta^2}}{Dt} - \frac{\partial}{\partial z} \left[ LqS_\theta \frac{\partial \overline{\theta^2}}{\partial z} \right] = -2\overline{w\theta} \frac{\partial \Theta}{\partial z} - \frac{2q}{B_2 L} \overline{\theta^2}. \tag{17}$$

Nomenclature for these equations follows that of Eq. 1 through 6 above, noting that  $S_q$  and  $S_\theta$  are dimensionless forms of their respective diffusion terms. A horizontally-homogeneous state is assumed for all mean variables. The mixing length,  $L$ , is diagnosed for the SBL according to the method described in N01 and based on

$$\frac{1}{L} = \frac{1}{L_S} + \frac{1}{L_T} + \frac{1}{L_B}, \tag{18}$$

where the three terms on the r.h.s. account for environmental stability, vertical profile of TKE, and buoyancy effects.

The variables  $A_1, A_2, B_1, B_2, C_1, C_2, C_3,$  and  $C_5$  are the MYNN closure parameters mentioned earlier. They act as weighting functions and determine the relative importance of shear or buoyancy terms in the production of turbulent energy or terms related to energy dissipation and energy redistribution among the three orthogonal directions of the system.

In the WRF model version 3.5.1, the closure-parameter values of the MYNN scheme (first row of Table 1) have been determined in previous works using observational and large-eddy simulation (LES) turbulence data and by invoking certain physical constraints based on

**Table 1** Suite of closure-parameter values used in the sensitivity experiments

Test	$A^1$	$A^2$	$B^1$	$B^2$	$C^1$	$C^2$	$C^3$	$C^4$	$C^5$
Control	1.18	0.67	24.00	15.00	0.14	0.73	0.34	0.00	0.20
50%	0.59	0.33	12.00	7.50	0.07	0.36	0.17	0.00	0.10
75%	0.89	0.50	18.00	11.25	0.10	0.55	0.26	0.00	0.15
200%	2.36	1.33	48.00	30.00	0.27	1.46	0.68	0.00	0.40

Values are systematically varied using 50, 75, and 200% of the control value (first row)

Monin–Obhukov theory that are applicable for the surface layer (MY82; NN04), but not necessarily for the full depth of the PBL. As is described in Sect. 3.2, however, closure-parameter values are systematically varied here without assuming any such physical dependencies or constraints to reveal changes in WRF-model wind-speed forecasts as related to changes to each closure parameter independently.

### 3 Methodology

A systematic set of experiments is formulated to investigate model sensitivities to changes in closure-parameter values. These closure-parameter values differ among the experiments, but remain constant throughout the forecast period of any one experiment. Discussed herein is the means for choosing a set of experimental cases from observations, the set-up of the mesoscale model, and the formulation of the suite of experiments.

#### 3.1 Selection of Wind-Ramp Cases

Wind-ramp cases are identified using observations from a tall tower near Hamburg, Germany operated by the Meteorological Institute of the University of Hamburg. Sonic anemometers at 50, 110, and 175 m above ground level (a.g.l.) provide the three-dimensional wind velocity components in orthogonal directions  $u$ ,  $v$ ,  $w$  with an accuracy of  $0.1 \text{ m s}^{-1}$  (Brummer et al. 2012). The data as provided are averaged temporally at 1-min resolution and consist of 3-years of data from 2010 to 2012. The TKE ( $q^2/2$ ) is available as a derived quantity from turbulent variance data at the vertical levels mentioned above.

Individual wind-ramp events are identified by a change in wind speed  $> 3 \text{ m s}^{-1}$  at 110-m height within 1 h or less. Because the focus here is the forecast of wind ramps in the context of the SBL and associated with the nocturnal LLJ, ramp events caused by other mechanisms such as frontal passage are excluded. Example observations for one case are given in Fig. 1. Five initial ramp cases are identified for the sensitivity experiments as described in the next section.

#### 3.2 Set-Up of WRF-Model Experiments

Wind-speed forecasts are generated using the WRF model, version 3.5.1. The Modern-era Retrospective Analysis for Research and Applications (MERRA) data files (Lucchesi 2012) are used for model boundary and initial conditions and are obtained from the National Aeronautics and Space Administration (NASA) Global Modeling and Assimilation Office through the Goddard Earth Sciences Data and Information Services Center. All forecasts are initialized at 1300 local time (LT = UTC + 1 h) on the first day of the respective case and end at

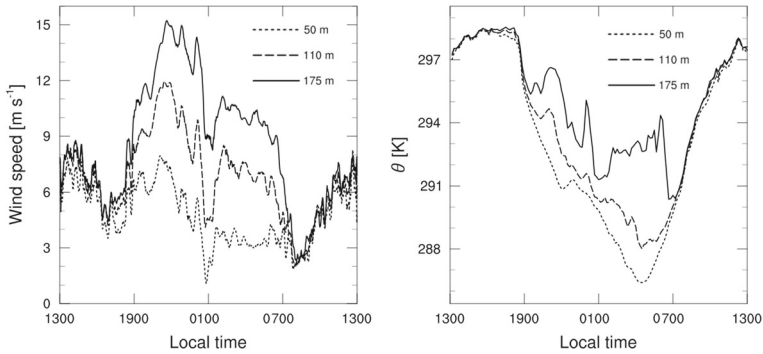
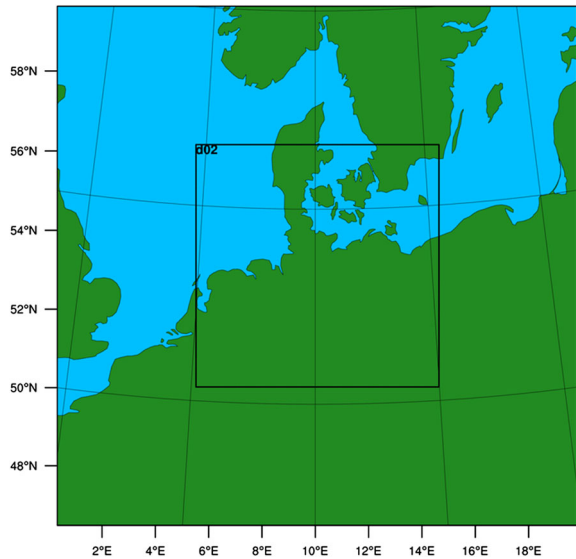


**Fig. 1** Observations of wind speed (*left panel*) and potential temperature (*right panel*) for the Hamburg case on 20 May 2012 for 50, 110, and 175 m

**Fig. 2** Nested domains used for the WRF model simulations



1300LT the following day (a 24-h forecast horizon). Two one-way nested grids are centred over Hamburg (Fig. 2) with horizontal grid spacings of 12 and 4 km respectively. Vertically, the domains use a stretched grid of 46 sigma levels up to 100 hPa. At, and below, 250 m, the specific levels in the model include 7.8, 21.6, 37.2, 52.9, 68.6, 84.4, 104.1, 133.7, 177.2, and 250.8 m [a.g.l.]. The MYNN level-3.0 scheme is used, which maintains a prognostic equation for temperature variance that is otherwise simplified to a diagnostic equation in the MYNN level-2.5 scheme. The Noah land-surface scheme (Chen and Dudhia 2001), and the WRF model single-moment 5-Class microphysical scheme (Hong et al. 2004) are used for all runs. The cumulus parametrization scheme of Kain–Fritsch (Kain 2004) is used only for the 12-km grid. Shortwave radiation processes are represented by the Dudhia scheme (1989) and longwave radiation by the rapid radiative transfer model (Mlawer et al. 1997).

For each of the wind-ramp cases, a suite of numerical forecasts is generated by systematically varying each closure parameter to be 50, 75, and 200% of its original value (Table 1). For any one forecast, only one closure parameter is changed; all other parameters are set

**Table 2** The MYNN closure parameters proposed by M73, MY82, and NN04 as well as the closure-parameter values in the WRF model version 3.5.1 for both the MYJ and MYNN schemes

	M73	MY82	NN04	WRF3.5—MYJ	WRF3.5—MYNN
$A_1$	0.78	0.92	1.18	0.66	1.18
$A_2$	0.79	0.74	0.665	0.657	0.67
$B_1$	15.0	16.6	24.0	11.88	24.0
$B_2$	8.0	10.1	15.0	7.227	15.0
$C_1$	0.056	0.08	0.137	0.00083	0.14
$C_2$			0.7		0.73
$C_3$			0.323		0.34
$C_4$			0.0		0.0
$C_5$			0.2		0.2

to their original MYNN value (the control). With each of eight closure parameters varied three times ( $C_4$  always remains zero) and including the original control forecast, the potential number of sensitivity experiments for one wind-ramp case is 25, and for the five cases, 125 experiments in all.

This range of closure-parameter values as in Table 1 is of the same order of the range of closure-constant values proposed in previous studies using the MYNN scheme (Table 2). Also listed are closure constants of the Mellor–Yamada–Janjic (MYJ) scheme (Janjic 1990, 1994) that, like the MYNN scheme, is also a 1.5-order turbulence closure scheme based on the approach of M73, MY74, and MY82, but with a different formulation of the turbulent mixing length.

## 4 Results

### 4.1 Varying $A_1$

For the first set of experiments, we vary  $A_1$  (first column, Table 1) while keeping all other closure parameters set to their respective original values (first row, Table 1). For the 4 September 2010 Hamburg case, where  $A_1$  is reduced to 75% of its original value, the forecast initial wind-ramp peak is  $1.5 \text{ m s}^{-1}$  higher than observed and the ramp down occurs 6 h too early (Fig. 3). When  $A_1$  is 50% its original value, the forecast initial wind-ramp peak is  $2.5 \text{ m s}^{-1}$  higher than observed, and the time of the ramp down is within 1 h of that observed. The control forecast does not produce a wind ramp and doubling  $A_1$  results in an overall decrease in wind speed over the forecast period.

All potential temperature forecasts for these same experiments exhibit cooling at the same rate starting around 1600 LT until 1900 LT, the time that coincides with ramp initiation at 110 m (Fig. 3). Thereafter there is some difference in evolution of the boundary layer among the four forecasts. The forecast that produces the strongest wind ramp (for which  $A_1$  is 50% of its original value) has no cooling after 1900 LT. When  $A_1$  is 75% of its original value, potential temperature decreases somewhat after 1900 LT, but less as compared to the control case and also produces a wind ramp stronger than the control.

Physical causes for these results are related to the evolution of turbulent momentum and heat fluxes (mixing) as well as TKE in the boundary layer and are discussed in Sect. 5.1.

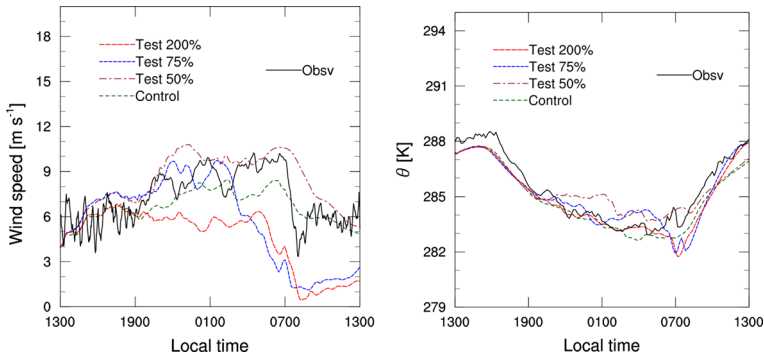


**Fig. 3** WRF model forecasts and observations of wind speed (*left panel*) and potential temperature (*right panel*) at a height of 110 m for the Hamburg 4 September 2010 case using the MYNN PBL scheme with values of  $A_1$  varied by 50, 75, and 200% of the control value (second column of Table 1)

**Table 3** Wind-speed forecast MAE values ( $\text{m s}^{-1}$ ) by case for varied  $A_1$  (left two columns)

Test	$A_1$	Cases by date					Average MAE
		10 July 2010	4 Sept 2010	25 April 2011	3 June 2011	20 May 2012	
Control	1.18	1.03/0	2.36/0	1.1/0	1.55/0	2.38/0	1.68/0
50%	0.59	1.11/8	1.04/−56	0.68/−39	1.10/−29	2.25/−5	1.24/−24
75%	0.89	0.55/−46	0.90/−62	0.74/−33	1.31/−15	2.12/−11	1.12/−34
200%	2.36	1.51/46	3.02/28	1.63/47	1.92/25	2.89/21	2.19/34

MAE is averaged over a 6-h period centred at the time of the wind ramp. In the remaining columns, the left number is the raw MAE value for the given experiment and the right number denotes the associated percentage change in wind-speed forecast MAE as compared to the control forecast (first row)

To evaluate the effect of varying  $A_1$  across all five cases, we calculated the mean absolute error (MAE) of the forecast 110-m wind speeds as compared to observations (Table 3). Here MAE values are averaged over a 6-h period centred at 1900LT, which is generally the time of wind-ramp initialization for the cases considered. We selected this 6-h time window so as to focus on forecast performance primarily during the development of the initial wind ramp (ramp-up). In general, the forecasts among the four experiments for any one wind-ramp case are highly similar *prior* to the wind ramp, thus allowing for more direct interpretation of effects *during* the ramp-up as caused by variations in the closure parameters. At the start of the ramp-down in the latter half of the forecast period, however, the environments among the experiments are already very different, making it difficult to ascertain the cause of forecast differences in the ramp-down as due either to initial conditions or to differences in closure-parameter settings.

To evaluate whether a change in  $A_1$  improves or degrades forecast accuracy, the percentage change in MAE values by variation of  $A_1$  is given in Table 3 (the right-hand number in each column). Setting  $A_1$  to 50% of its original value results in a lower forecast MAE for four of the five cases as compared to the control run, and three of these cases exhibit a MAE value that is reduced by more than 29%. All of the cases have a reduction in forecast MAE value when  $A_1$  is reduced to 75% of the control value, from an error 11–64% lower than the control forecast. Doubling  $A_1$  has an opposite effect, such that the forecast MAE value increases from 21 to 47% higher across the five wind-ramp cases as compared to their respective control forecasts.

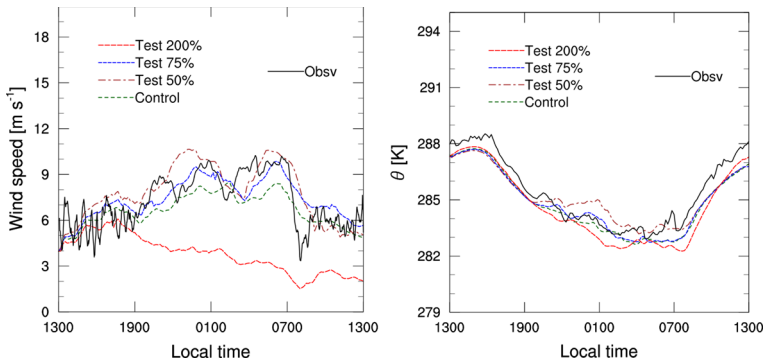


**Fig. 4** Same case as Fig. 3 but with forecast experiments based on varied  $B_1$

**Table 4** Same as Table 3 but showing wind-speed forecast  $MAE$  ( $m s^{-1}$ ) based on variations in  $B_1$

Test	$B_1$	Cases by date					Average $MAE$
		10 July 2010	4 Sept 2010	25 April 2011	3 June 2011	20 May 2012	
Control	24.0	1.03/0	2.36/0	1.1/0	1.55/0	2.38/0	1.68/0
50%	12.0	1.46/42	0.69/-71	0.65/-42	1.08/-30	1.92/-19	1.16/-24
75%	18.0	0.65/-37	1.31/-44	0.71/-36	1.26/-18	1.82/-23	1.15/-32
200%	48.0	2.64/156	4.23/79	2.59/134	2.84/83	3.49/47	3.16/100

### 4.2 Varying $B_1$

For the same case as analyzed in Sect. 4.1, decreasing  $B_1$  to 75 or 50% of its original value produces an increase in the wind-ramp peak of up to  $3 m s^{-1}$  at 110-m height as compared to the control (Fig. 4). When  $B_1$  is set to either 50 or 75% of the control value,  $MAE$  values are reduced on average across the five cases by 24 and 32% respectively (Table 4). Regarding potential temperature forecasts, experiments with greater forecast wind speeds (in Fig. 4 when  $B_1$  is 50 or 75% of its control value), there is less cooling of the boundary layer at 110 m after 1900LT as compared to the control.

The experiment for which  $B_1$  is doubled, no wind ramp is forecast, and the wind speed at 110 m decreases steadily over the 24-h forecast period (Fig. 4). This result is consistent for all five cases for which doubling  $B_1$  produces wind-speed forecasts that are on average 50% of the control forecast (not shown) and  $MAE$  values that are doubled (Table 4).

### 4.3 Varying $C_1$

Reducing  $C_1$  to 50 and 75% of its original value causes the forecasts to underpredict peak wind speeds at 110 m for the same Hamburg case as analyzed in the previous two sections (Fig. 5). In fact,  $MAE$  values for all five cases increase relative to the control forecast when  $C_1$  is reduced (Table 5). On average, the wind-speed forecast  $MAE$  value is 81% higher than the control forecast when  $C_1$  is reduced 50%, and 63% higher when  $C_1$  is set to 75% its original value.

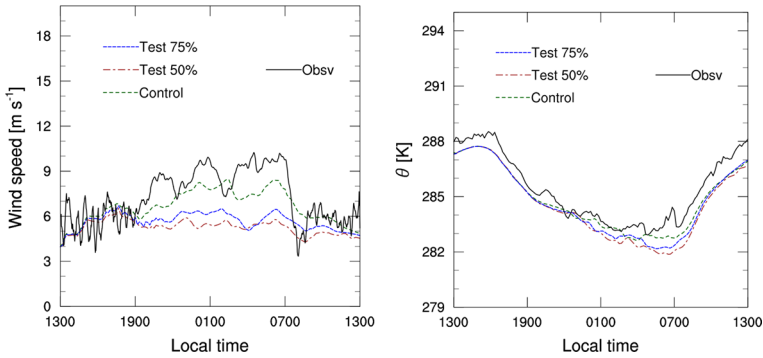


**Fig. 5** Same case as Figs. 3 and 4 but with forecast experiments based on varied  $C_1$

**Table 5** Same as Table 3 but for variations in  $C_1$

Test	$C_1$	Cases by date					Average <i>MAE</i>
		10 July 2010	4 Sept 2010	25 April 2011	3 June 2011	20 May 2012	
Control	0.14	1.03/0	2.36/0	1.10/0	1.55/0	2.38/0	1.68/0
50%	0.07	2.68/160	3.37/43	2.85/158	2.69/74	3.67/54	3.05/81
75%	0.10	2.99/190	3.03/28	2.22/101	2.29/48	3.24/36	2.75/63

Results for the WRF model forecasts using a value of  $C_1$  that is 200% of its control value were generally unstable and are not included here

Tests for which  $C_1$  is increased do not give conclusive results. Following convention as per the other closure parameters,  $C_1$  is increased by doubling its value. For these tests, however, the forecasts are often unstable and thus their results are not included in Fig. 5 or Table 5.

### 4.4 Varying Remaining Closure Parameters

An identical approach for evaluating forecast sensitivity to systematic changes in  $A_1$ ,  $B_1$ , and  $C_1$  is used to evaluate the forecast response to changes in the remaining closure parameters:  $A_2$ ,  $B_2$ ,  $C_2$ ,  $C_3$ , and  $C_5$ . Forecast sensitivities for these five closure parameters, although not negligible, are also not as significant as compared to  $A_1$ ,  $B_1$ , and  $C_1$ . Thus, the results of their respective experiments are not analyzed individually here, but rather included collectively in Fig. 6, for which percentage changes in wind-speed forecast *MAE* values are related to changes in respective closure parameters (50, 75, and 200% of the control value). Negative values in the figure indicate a reduction in *MAE* values and thus an improved forecast.

There is significantly higher forecast sensitivity to changes in  $A_1$ ,  $B_1$ , and  $C_1$  as compared to the other closure parameters. Generally, a reduction in the value of  $A_1$  or  $B_1$  to 50 or 75% of their original value causes a percentage reduction in *MAE* values up to 50%, while doubling these same closure parameters in some cases doubles forecast *MAE* values. Reducing  $C_1$  to 50 or 75% its original value always degrades forecasts, at times also doubling forecast *MAE* values. The effect on wind-speed forecasts due to variation in the remaining closure parameters is relatively less significant.

In the next section, a more in-depth analysis of the WRF-model forecast response to variations in closure-parameter values is given. Consideration is given primarily to the effect of changing the three most dominant closure parameters, namely  $A_1$ ,  $B_1$ , and  $C_1$ .

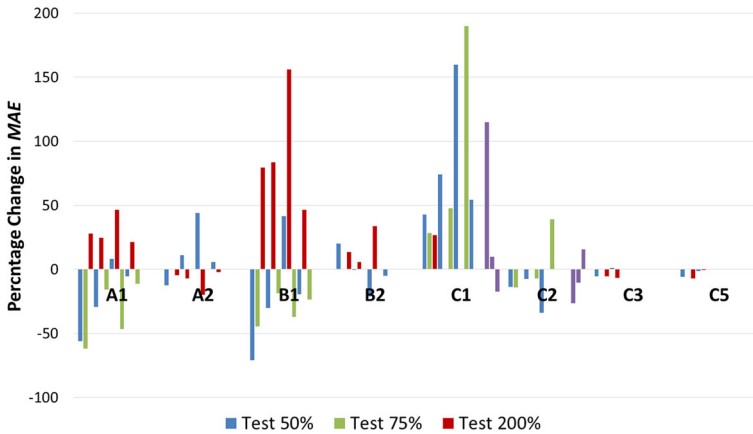


**Fig. 6** Percentage change in wind-speed forecast MAE values relative to the control forecast per individual change in each of the eight listed closure parameters

## 5 Analysis of Select Sensitivity Experiments

### 5.1 Impact of Changes to $A_1$

Analyzing the impact of the dominant closure parameters ( $A_1$ ,  $B_1$ , and  $C_1$ ) through Eqs. 7 to 15 is difficult due to the non-linearity of these equations. The parameter  $A_1$ , in particular, is a multiplicative factor for nearly all terms on the r.h.s. of Eq. 7 through 12, and it is difficult to isolate its influence. We present here a limited analysis based on the redistribution of the turbulent energy term,  $E_{distr,uw}$ , which is listed as a term in Eq. 4 that contributes to the overall evolution of the turbulent momentum flux. The term is given here specifically related to the turbulent momentum flux  $\overline{uw}$ ,

$$E_{distr,uw} = -\frac{q}{3A_1}\overline{uw} + C_1q^2\frac{\partial U}{\partial z}, \tag{19}$$

noting that  $E_{distr,uw}$  is neither an energy source nor sink term, but determines the redistribution of energy among the vertical and horizontal directions.

In Eq. 19, if  $A_1$  is reduced in value, the influence of the first term on the r.h.s. is increased ( $C_1$  remains unchanged), which in turn by Eq. 4 affects locally the turbulence momentum-flux field. Because the first term on the r.h.s. of Eq. 19 depends also on momentum flux (here  $\overline{uw}$ ), the process is highly non-linear. Referencing Eq. 2, which is rewritten here for both orthogonal components of the horizontal mean velocity and assuming only vertical gradients dominate,

$$\frac{\partial U}{\partial t} + \frac{\partial wU}{\partial z} = -\frac{1}{\rho}\frac{\partial P}{\partial x} + fV + \nu\nabla^2U - \frac{\partial\overline{uw}}{\partial z}, \tag{20}$$

and

$$\frac{\partial V}{\partial t} + \frac{\partial wV}{\partial z} = -\frac{1}{\rho}\frac{\partial P}{\partial y} - fU + \nu\nabla^2V - \frac{\partial\overline{vw}}{\partial z}, \tag{21}$$

an increase in  $-\partial(\overline{uw})/\partial z$  or  $-\partial(\overline{vw})/\partial z$  in turn should result in a local increase in mean wind speed.

The result of reducing  $A_1$  to 50% of its control value on the evolution of  $\overline{uw}$  is shown in Fig. 7b for one example case. (Here the  $\overline{vw}$  field is relatively small and not considered.) The

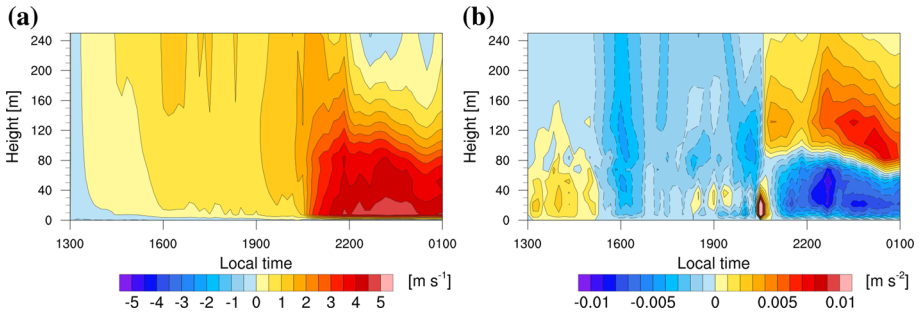


**Fig. 7** Contours show for the case on 4 September 2010 the difference as compared to the control forecast in the vertical profile of **a** wind speed ( $\text{m s}^{-1}$ ), and **b** the vertical gradient of momentum flux,  $\partial \overline{uw} / \partial z$  ( $\text{m s}^{-2}$ ), over the initial 12-h period when  $A_1$  is set to 50% its control value

gradient vector of the difference field prior to 2000LT is oriented horizontally and suggests the difference is caused by a time lag between the forecasts. Of significance to our analysis, however, is the development of a vertical gradient of  $\overline{uw}$ , which has a direct influence on the evolution of mean wind speed,  $U$ , per Eq. 20. Indeed, below 100-m height, there develops after 2000LT a negative vertical gradient of turbulent momentum flux  $-\partial(\overline{uw})/\partial z$  that is larger in the experiment for which  $A_1$  is 50% of its control value. This corresponds well with the placement of an increase in wind speed after 2000LT in Fig. 7a. It should be noted that on the l.h.s. of Eq. 20 is a term dependent on the vertical gradient of a flux term for the mean flow,  $\partial w/\partial z$ . The gradient of this flux term for this case, however, is nearly one order smaller than that of  $\overline{uw}$  and thus is less influential in forecast evolution (not shown).

Figure 8a shows warming between heights of 40 and 120 m and cooling at lower levels during the period after 2200LT when  $A_1$  is reduced to 50% of its control value. Such a trend increases the stability in the boundary layer, which would also tend to decrease turbulent mixing. This is consistent with Fig. 8b that shows a reduction in  $q^2/2$  (TKE) in the same area.

Causes for this warming trend can be linked to heat-flux terms as represented in the fundamental expression for potential temperature,

$$\frac{\partial \Theta}{\partial t} = -\frac{\partial}{\partial z} w\theta - \frac{\partial}{\partial z} \overline{w\theta} + \alpha \nabla^2 \Theta. \tag{22}$$

Figure 8d gives the difference field for the first term on the r.h.s. of Eq. 22 when  $A_1$  is set to half its original value, which involves the vertical gradient of the flux of mean potential temperature,  $w\theta$ . After 2200LT and between 40- and 120-m heights,  $\partial(w\theta)/\partial z$  is negative, which according to Eq. 22, would favour atmospheric warming and is thus consistent with the trend in potential temperature in Fig. 8a.

The second term on the r.h.s. of Eq. 22 involves the vertical gradient of turbulent heat flux,  $\overline{w\theta}$ . Figure 8d shows that  $\partial(\overline{w\theta})/\partial z$  has relatively high positive values in the same height and time as strong warming occurs (Fig. 8a). This trend is opposite what is dictated in Eq. 22 for warming to occur. Comparing Fig. 8c, d, the vertical gradient of mean potential temperature flux is nearly one order magnitude larger than the vertical gradient of turbulence heat flux and thus dominates in its effect on the evolution of potential temperature.

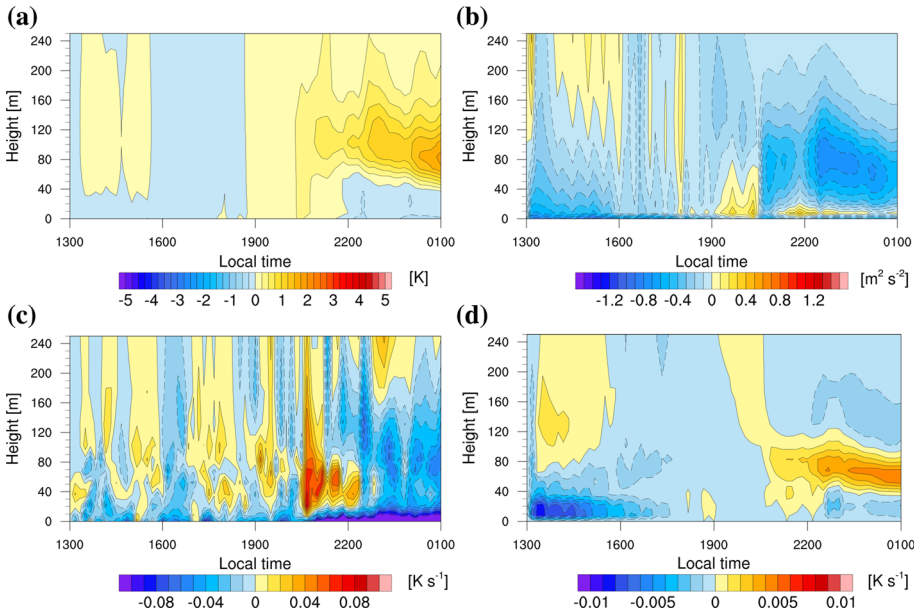


**Fig. 8** For the same case as Fig. 7 when  $A_1$  is reduced to 50% of control value, the difference in forecast vertical profiles over time are shown for: **a** potential temperature,  $\theta$  (K), **b** TKE,  $q^2/2$  ( $m^2 s^{-2}$ ), **c** vertical gradient of flux of the mean potential temperature,  $\partial w\theta/\partial z$  ( $K s^{-1}$ ), and **d** the vertical gradient of turbulence heat flux,  $\partial \overline{w\theta}/\partial z$  ( $K s^{-1}$ )

### 5.2 Impact of Changes to $C_1$

Because  $C_1$  directly affects only a limited number of terms, it is more straight-forward to ascertain the influence of  $C_1$  on wind-speed forecasts. Referencing as an example Eq. 11, the value of  $C_1$ , through the third term on the r.h.s., directly determines the flux  $\overline{uw}$ . From Eq. 20, however, what affects mean wind speed is not just  $\overline{uw}$ , but its vertical gradient. If we consider the change in  $\partial(\overline{uw})/\partial z$  only due to the change in the  $C_1$  term (Eq. 11),

$$\Delta \left( \frac{\partial \overline{uw}}{\partial z} \right) \equiv \Delta(C_1) \frac{\partial U}{\partial z} \frac{\partial q^2}{\partial z}, \tag{23}$$

where it is taken that the mean wind shear  $\partial U/\partial z > 0$ , and does not vary significantly with height at 100 m (as expected for the region below the LLJ maximum). Based on high-resolution numerical simulations of wind-ramp cases, it is generally found that a maximum in TKE ( $q^2/2$ ) occurs in the middle of the boundary layer and often below 100 m (not shown). As a result, it is assumed  $\partial q^2/\partial z < 0$  at 100 m, and thus the r.h.s. of Eq. 23 is negative and the l.h.s. is also negative. From Eq. 20, when  $\partial(\overline{uw})/\partial z < 0$ , wind speed increases. Thus when  $\Delta C_1$  is reduced, the amount that wind speed would have increased is also reduced. This theoretical argument is consistent with the trend in Fig. 9a such that the forecast wind speed at 110 m during and after the wind ramp (after 1900LT) is significantly reduced when  $C_1$  is reduced to half its original value.

Another approach is to analyze the impact of changes in  $C_1$  on the turbulent-flux fields themselves. Figure 9b shows the difference in the vertical gradient of  $\overline{uw}$  over time for a forecast with  $C_1$  set to half its original value as compared to the control forecast. The result

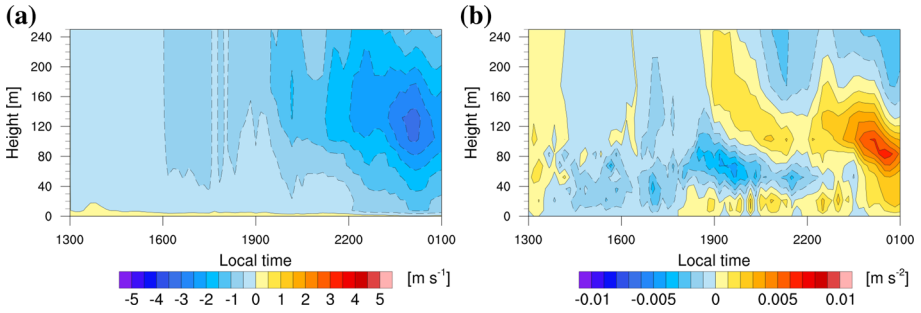


**Fig. 9** For the same case as Fig. 8 showing the difference in vertical profile of **a** wind speed ( $\text{m s}^{-1}$ ) and **b** the vertical gradient of momentum flux  $\overline{uw}$  ( $\text{m s}^{-2}$ ) when  $C_1$  is set to 50% of its original value

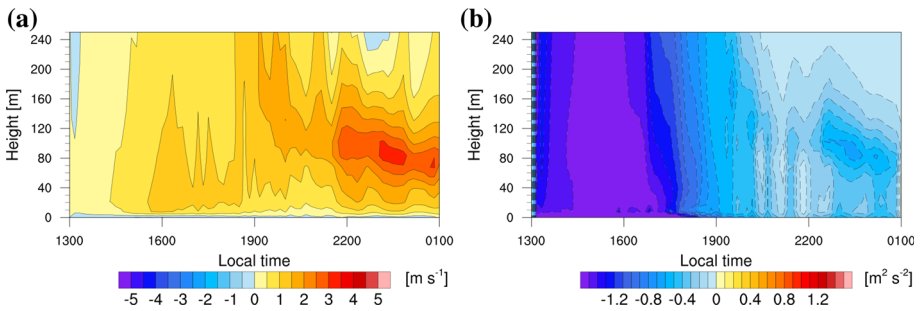


**Fig. 10** For the same case as Figs. 8 and 9, shown are the differences in vertical profile of **a** wind speed ( $\text{m s}^{-1}$ ) and **b**  $q^2/2$  ( $\text{m}^2 \text{s}^{-2}$ ) over a 12-h period when  $B_1$  is set to half its original value

appears very noisy; however, in the time period after 2300LT, there is evidence of an increase in the (positive) vertical gradient in the boundary layer between 40- and 140-m heights. Per Eq. 20, a larger positive field gradient,  $\partial(\overline{uw})/\partial z$ , causes a decrease in mean wind speed,  $U$ , an effect that is verified in Fig. 9a where there is a decrease in wind speed of over  $3 \text{ m s}^{-1}$  after 2200LT and between heights of 100 and 140m. There is not a significant difference in the mean potential temperature field among forecasts with varying  $C_1$  settings, and thus their results are not analyzed here.

### 5.3 Impact of Changes to $C_1$

The parameter  $B_1$  modulates the role of the dissipation term,  $E_{diss}$ , in Eq. 4. As given in MY82,

$$E_{diss} = -\frac{2q^3}{3LB_1}, \tag{24}$$

which acts to dissipate TKE and is nonzero only in Eq. 4 as posed for variance variables  $u^2$ ,  $v^2$ , and  $w^2$ . When  $B_1$  is set to half its original MYNN value, TKE ( $q^2/2$  in Fig. 10b) values are reduced after 2100LT. The largest change in  $q^2/2$  occurs at the same level as the largest increase in mean wind speed, near 100m. This makes physical sense in that dissipation acts to reduce turbulent energy, which reduces the effect of mixing that would otherwise allow for the transport of low momentum air to levels of higher momentum and thus reduce the strength of the LLJ. With  $B_1$  set to half its original value,  $q^2/2$  and thus mixing are reduced and a stronger LLJ is allowed to develop as compared to the control case.

## 6 Summary

For the set of wind-ramp cases considered, there was found a marked sensitivity in the WRF model wind-speed forecasts to variations in the values of closure parameters in the MYNN scheme, and in particular for changes to parameters  $A_1$ ,  $B_1$ , and  $C_1$ . Comparing WRF model forecasts with wind-speed observations at 110 m from a nearby tall tower, forecast *MAE* values were reduced between 11 and 64% when  $A_1$  was set to 75% of its original value and reduced 21–47% when  $B_1$  was set to 75% of its original value. Changes to other closure parameters did not result in such significant forecast improvement. Doubling the values of  $A_1$  or  $B_1$  uniformly degraded forecast accuracy at least 24%, while any change at all to  $C_1$  always produced worse forecasts.

These results underscore the problem of assuming the same closure parameters for the MYNN scheme regardless of environmental conditions. For wind-ramp cases in the SBL, there is evidence that modifying the closure parameters, even if only at the start of the forecast and maintaining them constant thereafter, creates an improvement in WRF model wind-speed forecasts. Subsequent work is called for in order to identify an optimal set of closure parameters for wind-ramp events.

**Acknowledgements** The work reported herein was supported by the US National Science Foundation (NSF) through its Integrated Graduate Education and Research Traineeship (IGERT) Program, award 1069283. Partial support was provided by the NSF also under the State of Iowa EPSCoR Grant 1101284 and by funds through the Iowa State University Foundation associated with the Pioneer Hi-Bred Agronomy Professorship. Partial support was also provided by NSF Grant AGS1624947. The tall-tower meteorological observations were provided through the Tall Tower Wind Measurement Project that was conducted by AWS Truepower and funded by the Iowa Energy Center and the US Dept. of Energy. The tall-tower data from Germany were provided through the Hamburg Meteorological Institute associated with the University of Hamburg. The High Performance Center at Iowa State University provided the bulk of computing resources that were used to run WRF and WRF-LES models for the suite of experiments. Appreciation is given to the reviewers, who provided insightful and helpful comments.

## References

- Benjamin S, Olson J, James E, Alexander C, Brown JM, Weygandt S, Smirnova T, Wilczak J (2013) Advances in model forecast skill from 2012–2013 assimilation and modeling enhancements to NOAA hourly updated models. In: UVIG workshop on forecasting applications, Salt Lake City
- Bruemmer B, Lange I, Konow H (2012) Atmospheric boundary layer measurements at the 280 m high Hamburg weather mast 1995–2011: mean annual and diurnal cycles. *Meteorol Z* 21:319–335
- Chen F, Dudhia J (2001) Coupling an advanced land surface-hydrology model with the Penn State-NCAR MM5 modeling system, part I: model implementation and sensitivity. *Mon Weather Rev* 129:569–585
- Deppe AJ, Wa G, Takle ES (2013) A WRF ensemble for improved wind speed forecasts at turbine height. *Weather Forecast* 28(1):212–228. doi:[10.1175/WAF-D-11-00112.1](https://doi.org/10.1175/WAF-D-11-00112.1)
- Dudhia J (1989) Numerical study of convection observed during the winter monsoon experiment using a mesoscale two-dimensional model. *J Atmos Sci* 46:3077–3107
- Fernando HJS, Weil JC (2010) Whither the stable boundary layer? A shift in the research agenda. *Bull Am Meteorol Soc* 91(11):1475–1484
- Greaves B, Collins J, Parkes J, Tindal A, Hassan G, Vincent S, Lane S (2009) Temporal forecast uncertainty for ramp events. *Wind Eng* 33(4):309–320
- Grisogono B (2010) Generalizing z-less mixing length for stable boundary layers. *Q J R Meteorol Soc* 136(646):213–221. doi:[10.1002/qj.529](https://doi.org/10.1002/qj.529)
- Hong SY, Dudhia J, Chen SH (2004) A revised approach to ice microphysical processes for the bulk parameterization of clouds and precipitation. *Mon Weather Rev* 132:103–120
- Hu XM, Klein P, Xue M (2013) Evaluation of the updated YSU planetary boundary layer scheme within WRF for wind resource and air quality assessments. *J Geophys Res* 118:1831–1844
- Janjic Z (1990) The step-mountain coordinate: physical package. *Mon Weather Rev* 118:1429–1443

- Janjic Z (1994) The step-mountain eta coordinate model: further developments of the convection, viscous sublayer, and turbulence closure schemes. *Mon Weather Rev* 122:927–945
- Kain JS (2004) The Kain–Fritsch convective parameterization: an update. *J Appl Meteorol* 43:170–181
- Lucchesi R (2012) File specification for MERRA products. Technical report, NASA Global Modeling and Assimilation Office, no. 1 version 2.3
- Mellor G, Yamada T (1974) Hierarchy of turbulence closure models for planetary boundary layers. *J Atmos Sci* 31:1791–1806
- Mellor GL (1973) Analytic prediction of the properties of stratified planetary surface layers. *J Atmos Sci* 30:1061–1069
- Mellor GL, Yamada T (1982) Development of a turbulence closure model for geophysical fluid problems. *Rev Geophys Space Phys* 20(4):851–875
- Mlawer EJ, Taubman SJ, Brown PD, Iacono MJ, Clough SA (1997) Radiative transfer for inhomogeneous atmospheres: RRTM a validated correlated-k model for the longwave. *J Geophys Res* 102:16663–16682
- Nakanishi M (2001) Improvement of the Mellor–Yamada turbulence closure model based on large-eddy simulation data. *Boundary-Layer Meteorol* 99:349–378
- Nakanishi M, Niino H (2004) An improved Mellor–Yamada level-3 model with condensation physics: its design and verification. *Boundary-Layer Meteorol* 112(1):1–31
- Navid N, Rosenwald G, Chatterjee D (2011) Ramp capability for load following in the MISO markets. Technical report 1, MISO market development and analysis. <https://www.misoenergy.org/Library/Repository/CommunicationMaterial/KeyPresentationsandWhitepapers/RampCapabilityforLoadFollowinginMISOMarketsWhitePaper.pdf>
- Schreck S, Lundquist J, Shaw W (2008) US department of energy workshop report: research needs for wind resource characterization. Technical report NREL/TP-500-43521, National Renewable Energy Laboratory
- Skamarock WC, Klemp J, Dudhia J, Gill DO, Barker DM, Duda MG, Huang XY, Wang W, Powers JG (2008) A description of the advanced research WRF version 3. Technical report, National Center for Atmospheric Research, NCAR Technical Note NAR/TN-475+STR, 113 pp
- Storm B, Basu S (2010) The WRF model forecast-derived low-level wind shear climatology over the United States Great Plains. *Energies* 3(2):258–276. doi:10.3390/en3020258